Chemical Science

ROYAL SOCIETY OF CHEMISTRY

EDGE ARTICLE

View Article Online
View Journal | View Issue

Cite this: *Chem. Sci.*, 2024, **15**, 11633

All publication charges for this article have been paid for by the Royal Society of Chemistry

Received 7th October 2023
Accepted 6th June 2024

DOI: 10.1039/d3sc05300h

rsc.li/chemical-science

Programmable "triple attack" cancer therapy through *in situ* activation of disulfiram toxification combined with phototherapeutics†

Qiu-Ling He,‡[a] Ben-Xu Jia,‡[ab] Zhi-Rong Luo,‡[d] Yu-Kun Wang,[b] Bo Zhang,[b] Tao Liao,[a] Xuan-Yi Guang,[b] Yan-Fang Feng,*[a] Zhen Zhang*[c] and Bo Zhou *[ab]

Effectively and completely eliminating residual tumor cells is the key to reducing the risk of tumor metastasis and recurrence. Designing an "ideal" nanoplatform for programmable cancer therapy has great prospects for completely eliminating residual tumor cells. Herein, an intelligent nanoplatform of disulfiram (DSF)-loaded CuS-tannic acid nanohexahedrons (denoted as "DSF-CuS@TA") with thermal- and pH-sensitive degradation, as well as near-infrared (NIR-II) phototherapeutics properties, was constructed. And then, it was employed for *in situ* DSF toxification activation programmable "triple attack" cancer therapy. After accumulating in the tumor, DSF-CuS@TA first releases the loaded $Cu(DTC)_2$, and simultaneously degrades and releases Cu^{2+} and DSF under mildly acidic stimulation to trigger instant intratumoral $Cu(DTC)_2$ chelation, thereby achieving the "first strike." Next, under irradiation by a NIR-II laser, light energy is converted into heat to generate NIR-II photothermal therapy, thereby achieving the second strike. Subsequently, under thermal stimulation, DSF-CuS@TA degrades further, triggering the chelation of $Cu(DTC)_2$ for a second time to reach the third strike. As expected, *in vitro* and *in vivo* studies showed that the synergistic integration of DSF-based programmed chemotherapy and NIR-II phototherapeutics could achieve effective tumor removal. Therefore, we propose a novel type of programmed therapy against cancer by designing a nanoplatform *via* "nontoxicity-to-toxicity" chemical chelation transformation.

Introduction

In recent years, phototherapeutics, as an efficient method for cancer diagnosis and treatment, has received widespread attention due to its sensitivity, non-invasiveness, low damage to normal tissue, high biocompatibility and precise spatiotemporal activation.[1–5] Unfortunately, due to the limited tissue penetration of the light source and temporary heat resistance formed by the synthesis of heat-related functional biomolecules (*e.g.*, heat shock proteins) under long-term high-temperature exposure, a small number of tumor cells can survive.[6–9] Residual tumor cells will remain, so patients are prone to metastasis and recurrence.[10,11] Therefore, there is an urgent need to find an efficacious treatment strategy combined with phototherapeutics to achieve accurate and efficient removal of residual cancer cells, thereby achieving complete tumor elimination.

Among numerous conventional therapeutic modalities, chemotherapy has been actively proposed for the development of tumor treatment systems with continuous cell-killing ability in combination with phototherapeutics.[12–16] The sustained killing of tumor cells is achieved through the controlled release of chemotherapy drugs, such as the release of photo-reactive drugs and tumor microenvironment (TME)-reactive drugs.[17–21] However, drug leakage and lack of targeting often lead to serious systemic toxicity and low bioactivity.[22–24] To meet the demand for "precision" medicine against cancers, programmed activation of chemotherapy drugs in a "nontoxicity-to-toxicity" manner is highly desirable.[25–29] However, lack of an "ideal" drug delivery system and specifically activated chemotherapy drug molecules pose challenges.[30,31] Therefore, searching for non-toxic or low-toxicity anticancer drugs and constructing an intelligent nanotheranostics platform to achieve precise activation of spatiotemporal programmed chemotherapy is crucial for removing residual cells and minimizing side effects.

Disulfiram (DSF) is an efficacious and inexpensive drug approved by US Food and Drug Administration (FDA) for the treatment of chronic alcoholism.[32–34] In recent years, it has been shown to have excellent therapeutic effects against cancer.[35–37] The anti-tumor activity of DSF is mainly manifested in the

[a]*School of Pharmacy, Guilin Medical University, Guilin, Guangxi, 541199, People's Republic of China. E-mail: 1328468450@qq.com; zb0909000021@163.com*

[b]*Scientific Research Center, Guilin Medical University, Guilin, Guangxi, 541199, People's Republic of China*

[c]*College of Intelligent Medicine and Biotechnology, Guilin Medical University, Guilin, Guangxi, 541199, People's Republic of China. E-mail: zhenzhang@glmc.edu.cn*

[d]*College of Chemistry and Environmental Engineering, Baise University, Baise, Guangxi 533000, People's Republic of China*

† Electronic supplementary information (ESI) available. See DOI: https://doi.org/10.1039/d3sc05300h

‡ These authors contributed equally to the work.

complex formed by chelation with Cu^{2+}. The addition of Cu^{2+} can greatly enhance the anti-tumor effect of DSF.[38] Cu^{2+} has a crucial role in enhancing DSF-based chemotherapy.[39–42] In the physiological environment, DSF is rapidly metabolized to diethyldithiocarbamate (DTC), which then chelates with Cu^{2+} to form a bis (*N*,*N*-diethyldithiocarbamate) copper(II) ($Cu(DTC)_2$) complex.[43–46] The highly cytotoxic $Cu(DTC)_2$ complex binds strongly to nuclear protein localization 4 (NPL4) and induces aggregation, thereby deactivating the p97-NPL4-UFD1 pathway and leading to apoptosis.[33,47,48] The endogenous level of copper in the TME is slightly higher than that in normal tissue, but it mainly exists in the valence of +1. Hence, the concentration of Cu^{2+} is too low to trigger the formation of $Cu(DTC)_2$ complexes.[38,49] To solve this problem, based on the excellent characteristics of a drug delivery system (especially nanomaterials with TME responsiveness), recently researchers have developed a nontoxicity-to-toxicity method for *in situ* Cu^{2+} chelation-enhanced tumor-specific chemotherapy.[50–52] By selectively transmitting and releasing Cu^{2+} at the tumor site, DTC chelates with Cu^{2+} and generates $Cu(DTC)_2$ *in situ*, thereby improving the efficacy of chemotherapy.[40,53,54] Inspired by the aforementioned preliminary work, we hypothesized that, if Cu^{2+} and DSF can be released at the tumor site based on the specific internal environment (*e.g.*, TME) and external stimulus programmatically, while DTC and Cu^{2+} chelate to generate $Cu(DTC)_2$ simultaneously for programmed therapy against tumors, a novel strategy for eliminating residual tumors could be created. Therefore, practitioners urgently need to design a nanosystem with multi-stimulus-responsive DSF and Cu^{2+} co-release to trigger *in situ* $Cu(DTC)_2$ generation for programmed chemotherapy and eliminate tumor residues completely.

Herein, an intelligent nanoplatform of DSF-loaded CuS-tannic acid nanohexahedrons (denoted as "DSF-CuS@TA") with near-infrared (NIR-II) phototherapeutics and thermo-sensitive and pH-sensitive degradation properties was constructed. This setup enabled *in situ* programmable activation of DSF toxification. Such "triple attack" therapy was employed to eliminate residual tumors. As shown in Scheme 1, after accumulating in the tumor, DSF-CuS@TA first releases loaded $Cu(DTC)_2$ and simultaneously degrades and releases Cu^{2+} *in situ* to trigger instant intratumoral $Cu(DTC)_2$ chelation under mildly acidic stimulation, thereby achieving the "first strike" (i). (ii) Next, under irradiation of the NIR-II laser, light energy is converted to heat to generate phototherapy, thereby achieving the second strike. (iii) Subsequently, under thermal stimulation, DSF-CuS@TA degrades further, triggering the chelation of $Cu(DTC)_2$ within the tumor to reach the third strike. Synergistic integration of DSF-based chemotherapy and NIR-II phototherapeutics can be realized *in vitro* and *in vivo* owing to the degradation properties of DSF-CuS@TA based on NIR-II photothermal as well as pH- and thermal stimulus responses. Therefore, this smart nanotherapeutic platform of DSF-CuS@TA was designed to achieve programmable triple-attack cancer therapy *via in situ* activation of DSF toxification. We designed a nanoplatform through a nontoxicity-to-toxicity method of chelation transformation. This is a novel strategy of programmed therapy against cancer.

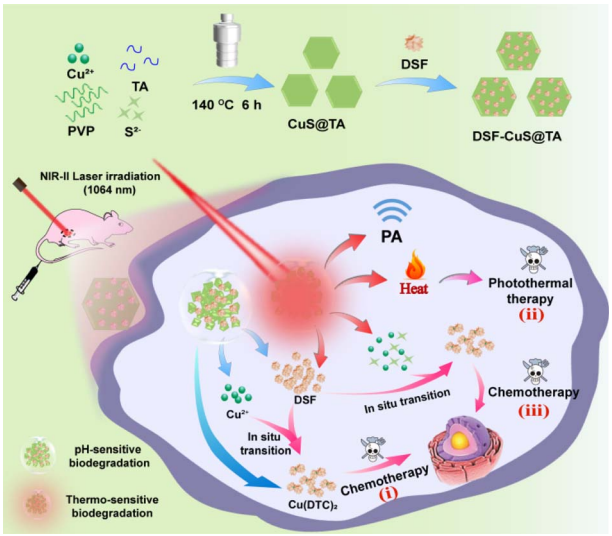

Scheme 1 Preparation of DSF-CuS@TA and corresponding programmed "triple attack" cancer therapy *via in situ* DSF toxification activation combined with phototherapeutics (schematic).

Results and discussion

Preparation and characterizations of DSF-CuS@TA

The preparation of DSF-CuS@TA included CuS@TA preparation and DSF encapsulation. First, CuS@TA were prepared *via* a one-step hydrothermal method. Then, the obtained CuS@TA were loaded with DSF to obtain DSF-CuS@TA (Scheme 1). Transmission electron microscopy (TEM) showed that CuS@TA exhibited regular nanohexahedrons with an average size of about 95.18 nm (Fig. 1a, inset). After loading with DSF, the morphology of DSF-CuS@TA was consistent with that of CuS@TA (Fig. 1b). Gaussian fitting revealed that the average size of DSF-CuS@TA was slightly larger than that of CuS@TA, with a particle size of approximately 112.41 nm (Fig. 1b, inset). Moreover, CuS@TA and DSF-CuS@TA exhibited the theoretical diffraction peaks of crystal CuS at 29.34°, 32.5°, 44.9°, and 47.8° measured by X-ray diffraction (XRD), indicating their synthesis (Fig. 1c). According to quantitative analysis, the encapsulation efficiency and loading efficiency of DSF were calculated to be 78.03% and 14.96%, respectively (Fig. S1†). Moreover, CuS@TA and DSF-CuS@TA exhibited excellent dispersibility in water, with hydrodynamic sizes of 184.6 nm and 208.7 nm, respectively (Fig. 1d). The zeta potential of CuS@TA and DSF-CuS@TA was determined to be −14.93 and −10.07 mV, respectively (Fig. S2†). The change in zeta potential of DSF-CuS@TA could be attributed to the encapsulation of positively charged DSF. In addition, the particle size of DSF-CuS@TA showed negligible changes, and there was no significant aggregation or precipitation in pure water, saline, PBS or alkaline media (RPMI 1640) within 24 h (Fig. S3†). These data indicated that DSF-CuS@TA had excellent colloidal stability, which was beneficial for subsequent biological applications.

FTIR and UV-vis-NIR were carried out to confirm that DSF were embedded in CuS@TA. FTIR spectroscopy of DSF-CuS@TA exhibited the stretching vibration of S–S, C=S and –N–C=S at

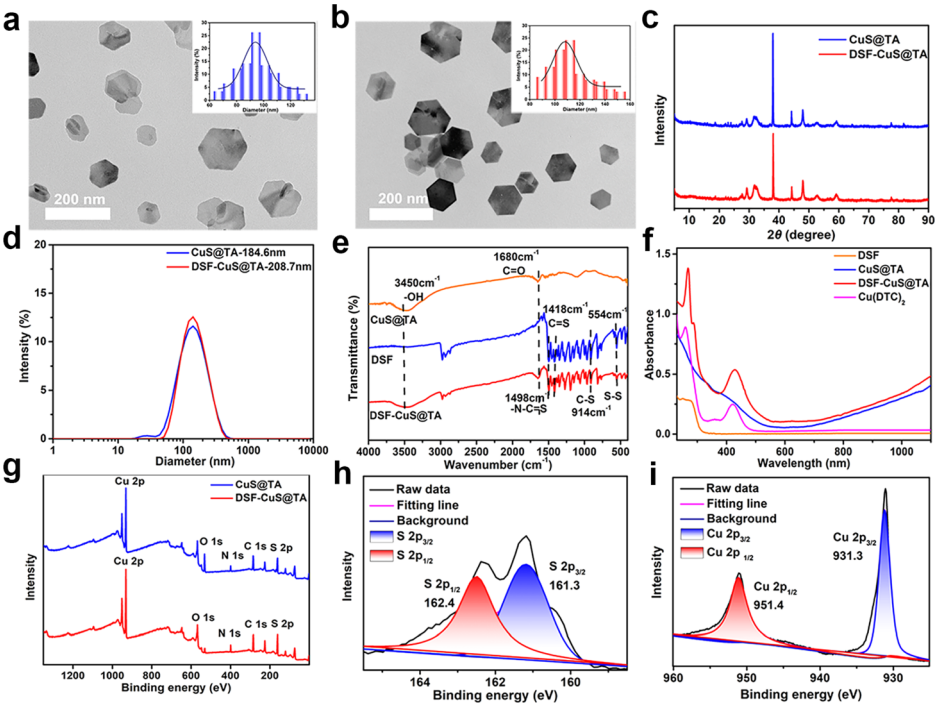

Fig. 1 Characterization of CuS@TA and DSF-CuS@TA. TEM images of (a) CuS@TA and (b) DSF-CuS@TA. Insets of (a) and (b) show the corresponding size distributions of CuS@TA and DSF-CuS@TA, respectively. (c) XRD pattern and (d) hydrodynamic size of CuS@TA and DSF-CuS@TA. (e) FTIR spectra of CuS@TA, DSF, and DSF-CuS@TA. (f) UV-vis-NIR spectra of DSF, CuS@TA, DSF-CuS@TA and $Cu(DTC)_2$. (g) XPS pattern of CuS@TA and DSF-CuS@TA, and the high-resolution (h) S 2p and (i) Cu 2p XPS pattern of DSF-CuS@TA.

554 cm^{-1}, 1418 cm^{-1} and 1498 cm^{-1}, respectively. Stretching vibration peaks corresponding to the C=O and –OH groups of TA appeared at 1680 cm^{-1} and 3650–3200 cm^{-1}, respectively (Fig. 1e).[25,55] From the UV-vis-NIR spectra, DSF-CuS@TA exhibited characteristic absorption with DSF in the range of 200 to 325 nm and showed characteristic absorption attributed to $Cu(DTC)_2$ at 265 nm and 425 nm (Fig. 1f).[26,56] These results indicated that DSF had become embedded in CuS@TA but also partially formed $Cu(DTC)_2$ complexes. Next, the chemical states of Cu and S within DSF-CuS@TA were analyzed by XPS. XPS showed that DSF-CuS@TA consisted of Cu, O, N, C and S elements (Fig. 1g). The binding energy of S $2p_{3/2}$ and S $2p_{1/2}$ at 161.3 and 162.2 eV implied the existence of sulfide and disulfide, respectively (Fig. 1h).[57,58] Characteristic peaks at 931.3 eV and 951.4 eV were consistent with the binding energies of Cu $2p_{3/2}$ and Cu $2p_{1/2}$, respectively,[51] suggesting that Cu in DSF-CuS@TA was in the form of divalent ions (Fig. 1i). According to elemental quantitative analysis using XPS, compared with CuS@TA, the amount of C and S elements in DSF-CuS@TA was increased significantly (Table S1†), further indicating the loading of DSF. Thus, all results indicated that CuS@TA had been prepared and DSF loaded effectively.

Photothermal and photoacoustic (PA) imaging properties of CuS@TA and DSF-CuS@TA

Inspired by the excellent photothermal performance of CuS,[59] further research was conducted on the photothermal performance of CuS@TA and DSF-CuS@TA. The photothermal properties of a material are dependent upon its characteristics of NIR absorption and performance of photothermal conversion. As presented in Fig. 2a, the absorbance of CuS@TA covered the NIR-II region, and its absorption intensity increased with an increase in its concentration. The extinction coefficient of CuS@TA at 1064 nm was calculated to be 17.5 L g^{-1} cm^{-1} (Fig. S4†), which featured efficient NIR-II photothermal conversion. Moreover, after DSF loading, there was no significant change in its absorption in the NIR-II biological window, demonstrating that the obtained DSF-CuS@TA had enormous potential application in photothermal conversion using a NIR-II laser (Fig. 2b). Based on these results, the performance of photothermal conversion of CuS@TA and DSF-CuS@TA under laser irradiation at 1064 nm was systematically explored. As shown in Fig. 2c and d, under laser irradiation at 1064 nm (1.0 W cm^{-2}), the temperature of aqueous solutions containing 20 μg mL^{-1} of CuS@TA and DSF-CuS@TA increased by 25 °C and 28 °C within 10 min, respectively, while the temperature of pure water increased by only 5 °C. In addition, CuS@TA and DSF-CuS@TA exhibited typical concentration- and power intensity-dependent photothermal conversion (Fig. 2e and f, S5a and b†). Meanwhile, due to their partial thermal degradation, after five cycles of heating and cooling, their photothermal properties showed a slight decrease (Fig. 2g and S5c†). These results indicated that CuS@TA could effectively and durably produce abundant heat upon NIR-II irradiation. Subsequently, according to the results of the cooling curve and heat transfer constant (Fig. 2h, S5d and S6†), the photothermal conversion efficiency (η) of CuS@TA and DSF-CuS@TA under laser irradiation at 1064 nm were 42.12% and 45.73%, respectively. These

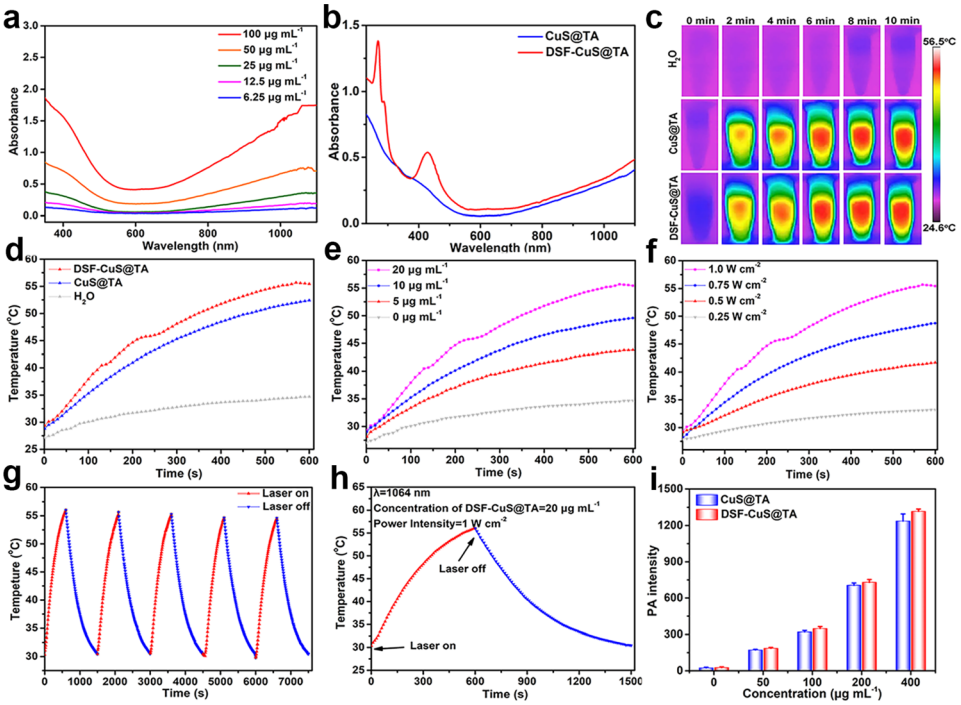

Fig. 2 Photothermal and PA imaging performances of CuS@TA and DSF-CuS@TA. (a) UV-vis-NIR absorption spectra of CuS@TA (6.25, 12.5, 25, 50, and 100 μg mL^{-1}) and (b) identical doses of CuS@TA and DSF-CuS@TA. (c) Photothermal images and (d) heating curves of CuS@TA, DSF-CuS@TA (20 μg mL^{-1}) and pure water. (e) Heating curves of different concentrations of DSF-CuS@TA upon 1064 nm laser (1.0 W cm^{-2}) exposure. (f) Heating curves of DSF-CuS@TA aqueous dispersion irradiated with a 1064 nm laser with different power densities. (g) Heating curve of DSF-CuS@TA under five cycles of heating and cooling processes. (h) Photothermal conversion capability of DSF-CuS@TA irradiated with a 1064 nm laser (1.0 W cm^{-2}). (i) PA values *versus* different concentrations of CuS@TA and DSF-CuS@TA.

results demonstrated that use of the NIR-II laser could lead to efficient conversion into heat mediated by CuS@TA and DSF-CuS@TA. It is worth noting that, due to the chelation of the DSF portion of the load with CuS@TA, brownish-black $Cu(DTC)_2$ was generated, which enhanced the absorption intensity of DSF-CuS@TA in the NIR-II region. Therefore, the η of DSF-CuS@TA was slightly higher than that of CuS@TA, exhibiting a better photothermal effect.

Due to the excellent photothermal performance of CuS@TA and DSF-CuS@TA, their PA imaging properties were also explored. As shown in Fig. 2i, with an increase in CuS@TA and DSF-CuS@TA concentrations, the PA signal increased significantly. This phenomenon corresponded to the PA image changing gradually from dark-blue to red and later gradually becoming darker (Fig. S7†). This result indicated that CuS@TA and DSF-CuS@TA had excellent PA imaging performance.

Thermal- and pH-triggered degradation characteristics and $Cu(DTC)_2$ generation behavior of DSF-CuS@TA

The thermal and tumor-specific degradation characteristics of CuS@TA had a crucial role in further activation of *in situ* DSF toxification. Neutral healthy body fluids and mildly acidic TME were simulated at pH of 7.4 and 6.5, respectively. The thermal and pH dual-stimulation degradation behavior of CuS@TA and DSF-CuS@TA were evaluated under incubation temperatures of 4 °C, 37 °C and 55 °C. As shown in Fig. 3a and b, S8,† the rate of reduction of particle size of CuS@TA and DSF-CuS@TA increased with a decrease in pH (from 7.4 to 6.5) and an increase in incubation temperature (from 4 °C to 55 °C). Under the stimulation of pH 6.5 and 55 °C, the particle size of CuS@TA decreased from 183.3 nm to 41.3 nm within 7 days (Fig. 3b). In addition, the UV-vis-NIR absorbance of CuS@TA at 1064 nm showed responsiveness to pH and thermal stimuli. Its absorption at 1064 nm decreased gradually with increasing incubation temperature and decreasing pH (Fig. 3c and d). To further confirm these results, CuS@TA was incubated in PBS at a pH of 7.4 and 6.5 under 55 °C for periods of time, then TEM images were collected. As expected, after being placed at pH 6.5 for 4 days, the morphology of CuS@TA began to deteriorate, with completely destruction noted after 7 days (Fig. 3e). In contrast, after 7 days at pH 7.4, the degree of morphological fragmentation of CuS@TA was relatively small. These results further demonstrated the degradation properties of CuS@TA in response to pH and heat. In addition, above presented results were confirmed by the intuitive color changes of the dispersion of CuS@TA. When the pH decreased from 7.4 to 6.5, as the incubation temperature and time increased, the color of the solution changed gradually from black to brown. After 7 days of cultivation at 55 °C and pH 6.5, the color of the solution was almost clear (Fig. S9†). Furthermore, the release of Cu^{2+} under different conditions of pH and incubation temperature were analyzed through ICP-OES. At the same incubation temperature, the release rate of Cu^{2+} from CuS@TA under mildly acidic conditions increased significantly compared with that under

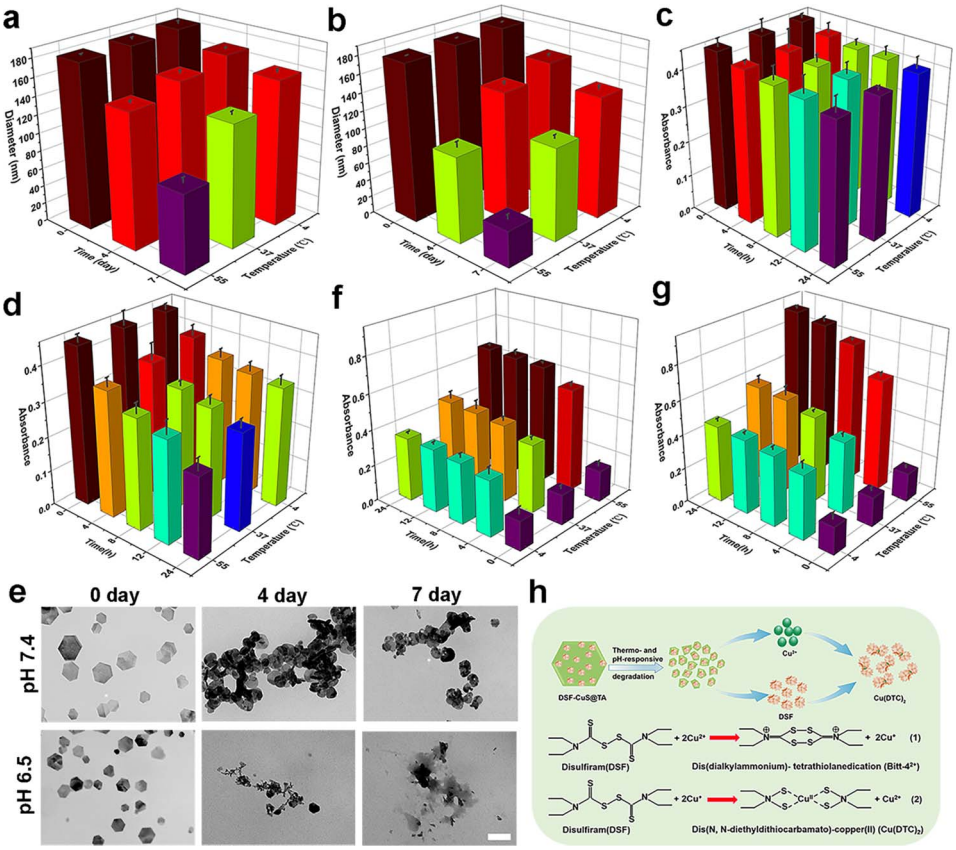

Fig. 3 Thermal- and pH- triggered degradation characteristics of CuS@TA. (a and b) Hydrodynamic size and (c and d) absorbance at 1064 nm of CuS@TA at pH 7.4 and 6.5, respectively. (e) TEM of CuS@TA at different time points under pH 7.4/6.5 and 55 °C incubation. Scale bar, 200 nm. Absorbance at 425 nm of DSF-CuS@TA at (f) pH 7.4 and (g) pH 6.5, respectively. (h) Biodegradation of DSF-CuS@TA and mechanisms of DSF/Cu^{2+} reactions, including DSF reduction by Cu^{2+} (schematic).

neutral conditions. At pH 6.5 and 55 °C, the release of Cu^{2+} reached over 80.57%, while at pH 7.4, only about 50.72% was released (Fig. S10†). All the above results indicated that CuS@TA had a unique pH and thermal dual-triggered degradation ability, allowing Cu^{2+} and DSF to be co-released under mildly acidic TME and external stimulation conditions.

Sequentially, the thermal- and pH-triggered formation of $Cu(DTC)_2$ *ex vitro* was carried out. After incubation at different pH (7.4 and 6.5) and temperatures (4 °C, 37 °C and 55 °C) for different times, the changes in absorbance of the characteristic absorption peak attributed to the $Cu(DTC)_2$ complex at 425 nm were monitored. As shown in Fig. 3f and g, at pH 7.4, as the incubation temperature increased, the absorbance at 425 nm of DSF-CuS@TA dispersed in PBS increased gradually over time, indicating the accumulation and formation of $Cu(DTC)_2$. Interestingly, the absorption was enhanced significantly at the same time point at pH 6.5 (Fig. 3g), indicating that the formation of $Cu(DTC)_2$ by DSF-CuS@TA could produce long-lasting therapeutic performance in mildly acidic TME and thermal stimulation. Therefore, the therapeutic concept of *in situ* conversion of DSF induced by CuS@TA to highly toxic $Cu(DTC)_2$ under specific mildly acidic and thermal stimulations was feasible *in vitro* (Fig. 3h).

In vitro programmed cell-killing efficacy

Primarily, to evaluate the efficiency of cellular uptake of CuS@TA, fluorescent reagent R6G was loaded into CuS@TA (denoted as "R6G-CuS@TA"). The characterization of R6G-CuS@TA is shown in Fig. S11.† Then, the fluorescence characteristic of R6G-CuS@TA was utilized to observe its efficiency of cellular uptake. As exhibited in Fig. S12,† after incubation for 4 h, the red fluorescence signal of R6G in 4T1 cells could be clearly observed and was enhanced during prolonged incubation (0–12 h), indicating that R6G-CuS@TA could be effectively internalized by cells. Moreover, the red fluorescence in 4T1 cancer cells was mainly distributed in the cytoplasm. Meanwhile, the content of Cu^{2+} in cells was further evaluated by ICP-OES to study the efficiency of cellular uptake. The internalization amounts of Cu^{2+} increased with the prolongation of incubation time (0–12 h), implying that CuS@TA could be efficiently internalized in a time-dependent manner (Fig. S13†).

The accelerated degradation behavior of DSF-CuS@TA under specific mildly acidic TME and thermal stimulation could effectively release Cu^{2+} and DSF. Based on these features, the thermally stimulated and mildly acidic TME could respond to $Cu(DTC)_2$ generated *in situ* to achieve programmed therapy of tumor cells (Fig. 4a). To verify this assumption, the

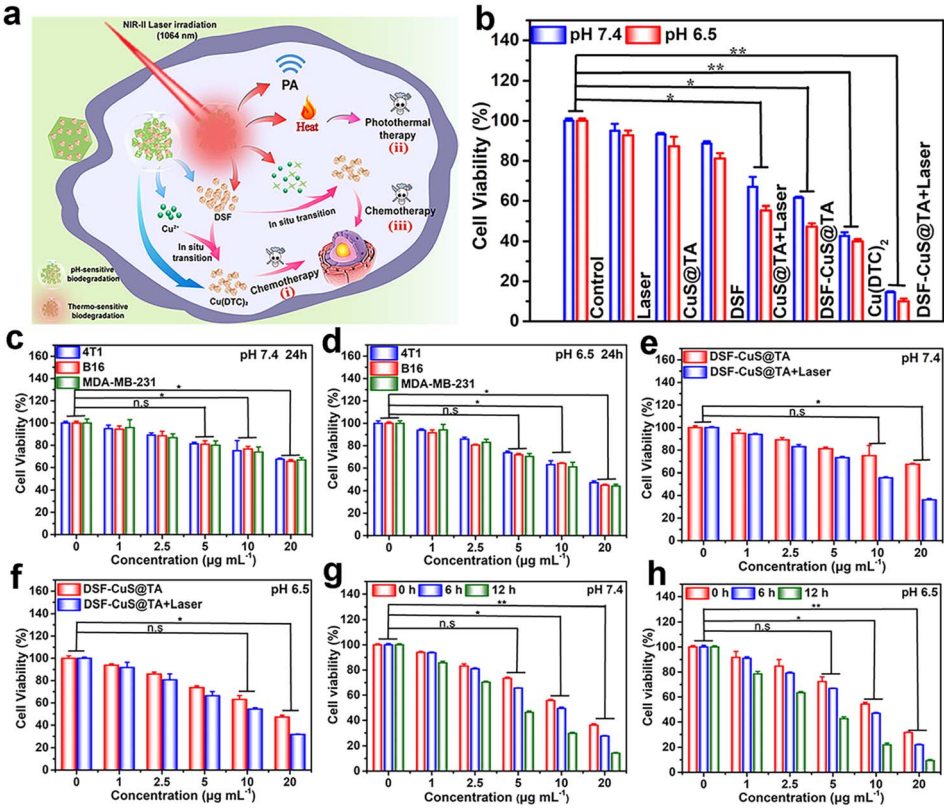

Fig. 4 (a) DSF-CuS@TA used for programmed "triple attack" against cancer cells (schematic). (b) Relative cell survival after different treatments: control, laser, CuS@TA, DSF, CuS@TA + Laser, DSF-CuS@TA, $Cu(DTC)_2$ and DSF-CuS@TA + Laser groups. Viability of 4T1 cells treated with different doses of DSF-CuS@TA under (c) pH 7.4 and (d) pH 6.5 for 24 h. Viability of 4T1 cells incubated with different doses of DSF-CuS@TA with or without of laser irradiation under (e) pH 7.4 and (f) pH 6.5. Viability of 4T1 cells incubated with different doses of DSF-CuS@TA with 1064 nm laser irradiation for 10 min and continuing incubation for an additional 0, 6, and 12 h under (g) pH 7.4 and (h) pH 6.5. Statistical significance was calculated *via* the Student's *t*-test. $*p < 0.05$ and $**p < 0.01$.

programmed triple attack against cancer cells *in vitro* was assessed using the MTT assay. Even if the dose of CuS@TA increased to 20 μg mL^{-1} at pH 6.5, and the treatment time was extended from 12 h to 24 h, the toxicity of CuS@TA and DSF to tumor (4T1, B16, and MDA-MB-231) cells could be ignored (Fig. S14 and S15†). Moreover, DSF-CuS@TA exhibited negligible toxicity to normal (L02 and 293T) cells at pH 7.4 (Fig. S16†). These results indicated the low toxicity of DSF, excellent cytocompatibility of CuS@TA, and low toxicity of DSF-CuS@TA to normal cells, respectively. Then, the first strike was undertaken by treating cells with DSF-CuS@TA for 12 h and 24 h under a mildly acidic TME. Under identical pH conditions, as the incubation time increased, the number of cells surviving decreased. Under the same time conditions as DSF-CuS@TA treatment of cells, the chemotherapy effect was significant at pH 6.5 (Fig. 4c and d, S17†). These data implied that the mildly acidic environment contributed to the release of $Cu(DTC)_2$ and *in situ* generation of $Cu(DTC)_2$, and $Cu(DTC)_2$ acted as a chemotherapeutic agent to achieve inhibition of cancer-cell proliferation. Subsequently, the synergistic therapeutic effects of the first and second strikes were studied by irradiating DSF-CuS@TA-incubated cells with the NIR-II laser and immediately testing cell viability. Compared with the first strike, the combination of irradiation using the NIR-II laser and first-strike chemotherapy significantly reduced cell viability (Fig. 4e and f). Programmed therapy using the triple attack was performed by irradiating DSF-CuS@TA-incubated cells with NIR-II laser and later continuing to culture for 6 h and 12 h. Interestingly, after continuous incubation for 6 h or 12 h, cell viability decreased gradually with an increase in the incubation time, demonstrating a sequential clearance effect on residual cancer cells (Fig. 4g and h). Thus, we concluded that triple-strike cancer therapy could be achieved based on the inherent NIR-II photothermal and thermal- and pH-response degradation characteristics of DSF-CuS@TA.

Furthermore, the overall synergistic therapeutic effect was studied through different cell treatments: control, Laser, CuS@TA, DSF, DSF + Laser, CuS@TA + Laser, DSF-CuS@TA, $Cu(DTC)_2$ and DSF-CuS@TA + Laser groups (Fig. 4b and S18†). As shown in Fig. 4b, only 12% of 4T1 cells remained alive after being treated with 20 μg mL^{-1} of DSF-CuS@TA under laser irradiation at 1064 nm (DSF-CuS@TA + Laser), while 44.2% and 55.3% of cells survived after being treated with free $Cu(DTC)_2$ and CuS@TA with laser exposure at 1064 nm (CuS@TA + Laser), indicating the stronger efficacy of synergistic anticancer therapy. Moreover, the cytotoxicity of various treatments on B16 and MDA-MB-231 cells was similar to that documented for 4T1 cells (Fig. S18 and S19†).

We wished to further identify the synergistic effect of NIR-II phototherapy combined with *in situ* thermal- and TME-triggered programmed chemotherapy. Annexin V-FITC and PI assays were performed after different treatments. As shown in Fig. 5a and S20,† compared with CuS@TA treatment and exposure to laser irradiation at 1064 nm for 10 min (25.01%), treatment with DSF-CuS@TA induced 69.17% of cells to undergo apoptosis. Meanwhile, after treatment with DSF-CuS@TA alone, 47.2% of cells underwent apoptosis. These results confirmed that synergistic chemotherapy and photothermal therapy (PTT) caused a significant number of tumor cells to die. Comparing the groups of cells treated with DSF-CuS@TA after laser irradiation and continuous incubation for different times revealed that DSF-CuS@TA could be used to achieve programmed tumor therapy (Fig. 5a). In addition, calcein AM/PI staining was performed to visualize the therapeutic effect. As shown in Fig. 5b, bright-green fluorescence (calcein-AM, alive cells) signals were distinctly observed in control, CuS@TA, DSF and 1064 nm laser groups, which further revealed that treatment with CuS@TA, DSF or a laser exhibited no obvious damage to 4T1 cancer cells. In contrast, bright-red fluorescence (dead cells under PI staining) was visualized in the group treated with DSF-CuS@TA under 1064 nm laser irradiation (DSF-CuS@TA + Laser), especially with prolonged continuous incubation after 1064 nm laser irradiation under pH 6.5, thereby exhibiting excellent time-dependent programmed cytotoxicity (Fig. S21†). Moreover, green fluorescence and red fluorescence could be observed in $Cu(DTC)_2$, DSF-CuS@TA and CuS@TA + Laser groups, indicating that a combination of PTT and chemotherapy had a better therapeutic effect.

Combined antitumor effect *in vivo*

Encouraged by the *in vitro* synergistic effect of PTT and *in situ* chemotherapy, the *in vivo* therapeutic efficacy of DSF-CuS@TA was systematically assessed. First, R6G-CuS@TA was employed to investigate the accumulation and biodistribution of DSF-CuS@TA *in vivo*. After intravenous injection, the *in vivo* fluorescence images of R6G-CuS@TA were recorded at different time intervals by the IVIS® system. Initially, with a change of time, obvious fluorescence appeared at the tumor site 4 h after injection, and increased gradually within 12 h. Compared with main organs, tumor tissue had a clear fluorescence signal, indicating that DSF-CuS@TA had long retention and favorable intratumoral enrichment (Fig. 6a). Moreover, based on the outstanding photothermal-conversion capability of CuS@TA and DSF-CuS@TA, PA imaging *in vivo* was performed. As displayed in Fig. 6b, PA imaging of the tumor site changed from dark to red at different times post-injection, and the signal at tumor regions exhibited a time-dependent pattern (Fig. S22†). These data indicated that DSF-CuS@TA could be effectively enriched and enhanced PA imaging at the tumor site.

Subsequently, given that favorable biocompatibility and accumulation in tumor tissues had been confirmed, the synergistic effect of NIR-II PTT combined with *in situ* thermal- and TME-triggered programmed chemotherapy *in vivo* of DSF-CuS@TA was comprehensively evaluated. The 4T1 tumor-bearing mouse model was used. Mice were assigned into eight groups randomly: control, Laser (saline + Laser), CuS@TA, DSF, CuS@TA + Laser, DSF-CuS@TA, $Cu(DTC)_2$, and DSF-CuS@TA + Laser. Among them, tumor tissue in the photothermal treatment group was irradiated by a 1064 nm laser for 10 min after

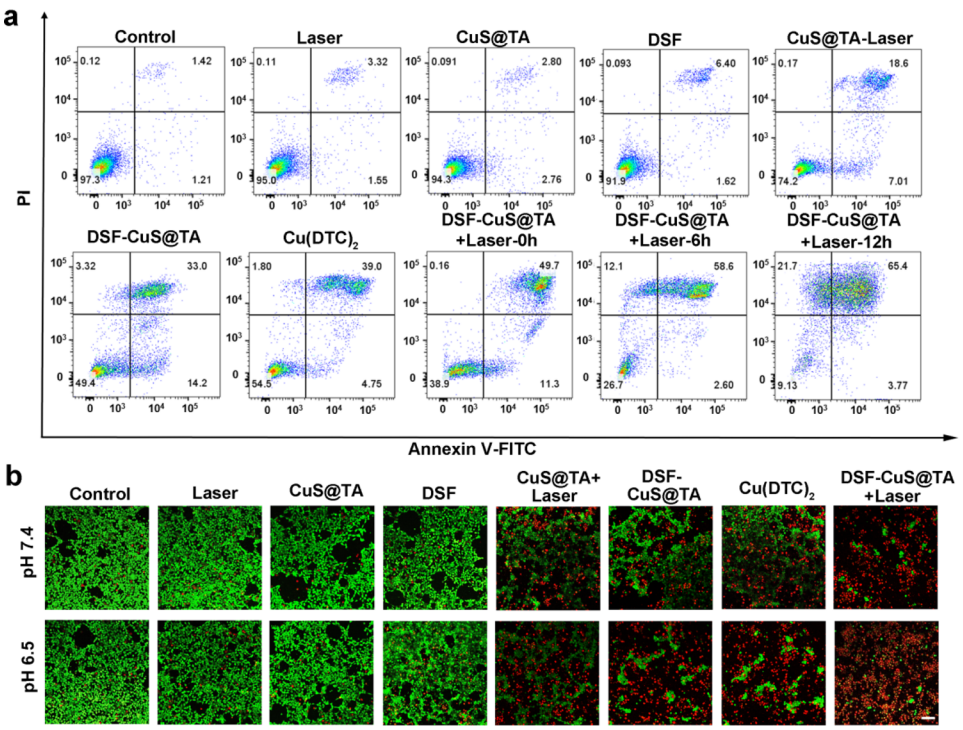

Fig. 5 (a) Flow cytometry based on staining (Annexin-FITC and PI) after different treatments and (b) CLSM images of 4T1 cells labeled with calcein-AM and PI. Scale bar, 100 μm.

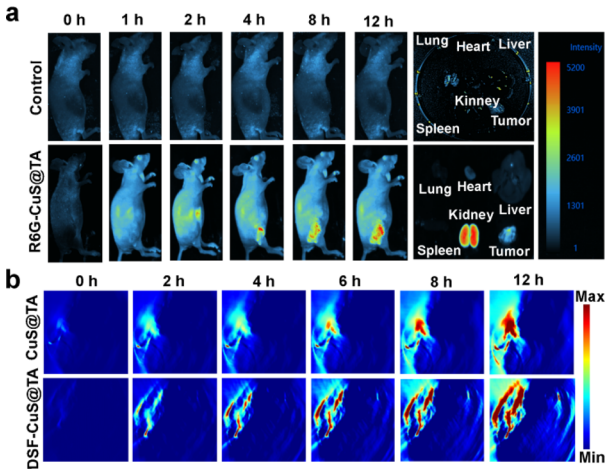

Fig. 6 (a) *In vivo* fluorescence images of 4T1 tumor-bearing BALB/c nude mice captured at different time points after intravenous injection of R6G-CuS@TA, as well as fluorescence imaging of main organs and tumor tissues 12 h after injection. (b) *In vivo* PA imaging of the tumor position after intravenous injection of CuS@TA and DSF-CuS@TA for different times.

injection of saline/CuS@TA/DSF-CuS@TA for 12 h, and temperature changes and photothermal images of the tumor were recorded using a temperature recorder and thermal imager, respectively. As shown in Fig. 7a and b, the tumor temperature in the 1064 nm laser group increased by only 2 °C. In contrast, the temperature in the CuS@TA + Laser and DSF-CuS@TA + Laser groups reached up to 53.7 and 55.6 °C, respectively. As shown in Fig. 7c and S23,† in the 14 days of treatment, single employment of DSF, CuS@TA and laser irradiation did not show any suppressive effect on tumor growth. In contrast, tumor growth in the CuS@TA + Laser and DSF-CuS@TA groups was inhibited to a certain extent. Importantly, the trend in tumor volume showed that the DSF-CuS@TA + Laser irradiation had a significant inhibitory effect on tumor proliferation, with percent inhibition up to 77.48% (Fig. 7d), which was higher than that of the other groups (Fig. 7e). Hence, a combination of PTT and *in situ* $Cu(DTC)_2$ chemotherapy could suppress tumor propagation. In addition, the body weight of mice in all the treatment groups during the entire treatment period showed no significant change (Fig. 7f). This result indirectly indicated that DSF-CuS@TA had therapeutic safety.

To evaluate therapeutic efficacy further, after various treatments, H&E staining was carried out. Tumor tissues in the DSF-CuS@TA, $Cu(DTC)_2$ and CuS@TA + Laser groups exhibited significant apoptosis/necrosis. Notably, the degree of apoptosis and necrosis in the DSF-CuS@TA + Laser irradiation group was significantly higher than that in the other treatment groups (Fig. 7g). Moreover, H&E staining reveal no tissue damage in the major organs of mice of all treatment groups (Fig. S24†). Therefore, the DSF-CuS@TA nanoplatform with thermal- and TME-response degradation characteristics could achieve a combination of PTT- and DSF-based *in situ* programmed chemotherapy to realize precise cancer elimination. In

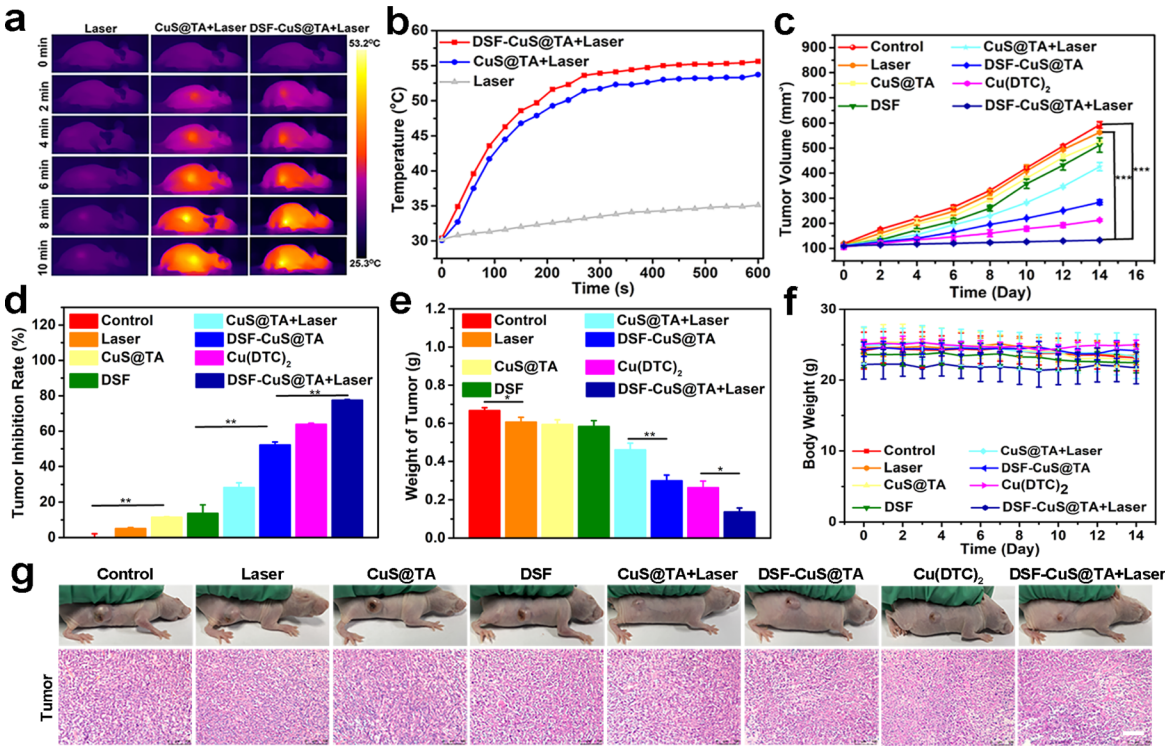

Fig. 7 (a) *In vivo* photothermal images and (b) heating curves of 4T1 tumor-bearing mice treated with saline, CuS@TA or DSF-CuS@TA under 1064 nm laser irradiation within 10 min. (c) Tumor volume, (d) percent tumor inhibition, (e) tumor weight, (f) body weight and (g) photographs and H&E staining of tumor tissues of 4T1 tumor-bearing mice in different treatment groups. Scale bar, 100 μm. Statistical significance was calculated *via* the Student's *t*-test. *p < 0.05, **p < 0.01, and ***p < 0.001.

addition, it should be pointed out that CuS, as an attractive photodynamic therapy (PDT) reagent and Cu^{2+} donor, has been widely studied in the PDT and chemodynamic therapy of tumors.[60–62] Therefore, combining the above characteristics with these will provide a new strategy for multifunctional tumor treatment.

Conclusions

In summary, we have successfully constructed a nanoplatform of CuS@TA with thermal and mildly acidic TME dual-stimulus response degradation. We realized DSF encapsulation, as well as programmed therapy based on NIR-II phototherapeutics and *in situ* activation of DSF toxification. Based on the inherent characteristics of CuS@TA, DSF-CuS@TA degraded and released sufficient Cu^{2+} and DSF within a tumor under a mildly acidic TME and thermal stimulation. This action immediately triggered intratumoral $Cu(DTC)_2$ chelation, thereby achieving sustained and efficient synergistic NIR-II phototherapeutics and programmed chemotherapy. *In vitro* and *in vivo* experiments demonstrated that this therapeutic nanoplatform could significantly inhibit tumor growth, thereby confirming its feasibility. Therefore, this designed and constructed DSF-CuS@TA through nontoxicity-to-toxicity chemical chelation transformation represents a promising nanoplatform and could be used to treat different cancer types.

Data availability

The authors declare that all data supporting the findings of this study are available from the corresponding author upon reasonable request. Cell lines, Mouse breast cancer (4T1) cells, human liver cells (L02), human kidney cells (293T), mouse melanoma cells (B16) and human breast cancer cells (MDA-MB-231) were acquired from the Chinese Academy of Sciences Cell Bank (Shanghai, China). An experimental model using SPF-grade female BALB/c mice was provided by Hunan Slack Jingda Laboratory Animal Co. All animal experiments were performed in accordance with the guidelines of Institutional Animal Care and Use Committee and set by the Laboratory Animal Care and Animal Ethics Committee of Guilin Medical University (GLMC-IACUC-2022027).

Author contributions

Qiu-Ling He: methodology, investigation, data curation, and writing original draft. Ben-Xu Jia: investigation, data curation, and writing original draft. Zhi-Rong Luo: investigation, methodology, and data curation. Yu-Kun Wang: methodology and data curation. Bo Zhang: methodology and data curation. Tao Liao: investigation and data curation. Xuan-Yi Guang: investigation and data curation. Yan-Fang Feng: conceptualization, writing – review & editing, and funding acquisition. Zhen Zhang: supervision, resources, writing – review & editing, and funding acquisition. Bo Zhou: supervision, conceptualization, resources, writing – review & editing, and funding acquisition.

Conflicts of interest

The authors declare no conflicts of interest.

Acknowledgements

This work was supported by Natural Science Foundation of Guangxi (2022GXNSFBA035620 and 2020GXNSFBA297026), National Natural Science Foundation of China (32060139) and Innovation Project of Guangxi College Students Education (S202210601140, S202310601202, S202310601107 and S202310601148).

References

1 C. Chen, H. Ou, R. Liu and D. Ding, *Adv. Mater.*, 2020, **32**, 1806331.
2 Z. Yang and X. Chen, *Acc. Chem. Res.*, 2019, **52**, 1245–1254.
3 H. Zhang, C. Zhu, J. Liang, S. Li, L.-F. Hu, H. Liang, W.-S. Kuo and X.-C. Shen, *Chem.–Eur. J.*, 2023, **29**, e202203196.
4 Y. Liu, Q. Guo, X. Zhu, W. Feng, L. Wang, L. Ma, G. Zhang, J. Zhou and F. Li, *Adv. Funct. Mater.*, 2016, **26**, 5120.
5 X. Li, J. F. Lovell, J. Yoon and X. Chen, *Nat. Rev. Clin. Oncol.*, 2020, **17**, 657–674.
6 R. Gomez-Pastor, E. T. Burchfiel and D. J. Thiele, *Nat. Rev. Mol. Cell Biol.*, 2018, **19**, 4–19.
7 J. Trepel, M. Mollapour, G. Giaccone and L. Neckers, *Nat. Rev. Cancer*, 2010, **10**, 537–549.
8 A. S. Lee, *Nat. Rev. Cancer*, 2014, **14**, 263–276.
9 Y. Wang, D. Cai, H. Wu, Y. Fu, Y. Cao, Y. Zhang, D. Wu, Q. Tian and S. Yang, *Nanoscale*, 2018, **10**, 4452–4462.
10 L. Zhang, A. Yang, C. Ruan, B.-P. Jiang, X. Guo, H. Liang, W.-S. Kuo and X.-C. Shen, *ACS Appl. Mater. Interfaces*, 2023, **15**, 3253–3265.
11 H. Xiong, X. Li, P. Kang, J. Perish, F. Neuhaus, J. E. Ploski, S. Kroener, M. O. Ogunyankin, J. E. Shin, J. A. Zasadzinski, H. Wang, P. A. Slesinger, A. Zumbuehl and Z. Qin, *Angew. Chem., Int. Ed.*, 2020, **59**, 8608–8615.
12 Z. Ren, S. Sun, R. Sun, G. Cui, L. Hong, B. Rao, A. Li, Z. Yu, Q. Kan and Z. Mao, *Adv. Mater.*, 2020, **32**, e1906024.
13 Z. Tian, C. Shen, J. Li, E. Reit, Y. Gu, H. Fu, S. A. Cummer and T. J. Huang, *Adv. Funct. Mater.*, 2019, **29**, 1808489.
14 Y. Wang, L. An, J. Lin, Q. Tian and S. Yang, *Chem. Eng. J.*, 2020, **385**, 123925.
15 X. Zhu, J. Li, X. Qiu, Y. Liu, W. Feng and F. Li, *Nat. Commun.*, 2018, **9**, 2176.
16 C. Yang, M. R. Younis, J. Zhang, J. Qu, J. Lin and P. Huang, *Small*, 2020, **16**, 2001518.
17 J. S. Conteh, G. E. P. Nucci, T. Fernandez Cabada, B. T. Mai, N. Soni, F. De Donato, L. Pasquale, F. Catalano, M. Prato, L. Manna and T. Pellegrino, *ACS Appl. Mater. Interfaces*, 2023, **15**, 22999–23011.
18 C. Zhu, Z. Guo, A. Yang, B.-P. Jiang, H. Liang and X.-C. Shen, *Inorg. Chem. Front.*, 2022, **9**, 1869–1878.
19 R. Ouyang, P. Cao, P. Jia, H. Wang, T. Zong, C. Dai, J. Yuan, Y. Li, D. Sun, N. Guo, Y. Miao and S. Zhou, *Bioact. Mater.*, 2021, **6**, 386–403.

20 J. Mao, Y. Li, Q. Cai, Z. Tang, Y. Yang, C. Yuan, Y. Xu, B. Zeng, W. Luo, S. Kuo and L. Dai, *Chem. Eng. J.*, 2021, **405**, 126690.
21 J. Zhu, Y. Zhang, Z. Li, X. Bao, Y. Zhou, B. Ma, Y. Xie, P. Yan, Z. Wu, Q. Zhang, J. Zou and X. Chen, *Mater. Horiz.*, 2023, **10**, 3014–3023.
22 S. Zhai, X. Hu, Z. Ji, H. Qin, Z. Wang, Y. Hu and D. Xing, *Nano Lett.*, 2019, **19**, 1728–1735.
23 Y. Cai, H. Shen, J. Zhan, M. Lin, L. Dai, C. Ren, Y. Shi, J. Liu, J. Gao and Z. Yang, *J. Am. Chem. Soc.*, 2017, **139**, 2876–2879.
24 H. Lin, Y. Chen and J. Shi, *Chem. Soc. Rev.*, 2018, **47**, 1938–1958.
25 X. Meng, K. Jia, K. Sun, L. Zhang and Z. Wang, *Chem. Eng. J.*, 2021, **415**, 128947.
26 W. Wu, L. Yu, Q. Jiang, M. Huo, H. Lin, L. Wang, Y. Chen and J. Shi, *J. Am. Chem. Soc.*, 2019, **141**, 11531–11539.
27 Y. Yang, J. Huang, W. Wei, Q. Zeng, X. Li, D. Xing, B. Zhou and T. Zhang, *Nat. Commun.*, 2022, **13**, 3149.
28 H. Zhang, F. Song, C. Dong, L. Yu, C. Chang and Y. Chen, *J. Nanobiotechnol.*, 2021, **19**, 290.
29 Z. Zhang, M. K. G. Jayakumar, X. Zheng, S. Shikha, Y. Zhang, A. Bansal, D. J. J. Poon, P. L. Chu, E. L. L. Yeo, M. L. K. Chua, S. K. Chee and Y. Zhang, *Nat. Commun.*, 2019, **10**, 4586.
30 J. Zhou, Y. Liu, G. Zhang, Q. Jia and L. Li, *Biomaterials*, 2019, **219**, 119395.
31 H. Chen, W. Zhang, G. Zhu, J. Xie and X. Chen, *Nat. Rev. Mater.*, 2017, **2**, 17024.
32 R. Bista, D. W. Lee, O. B. Pepper, D. O. Azorsa, R. J. Arceci and E. Aleem, *J. Exp. Clin. Cancer Res.*, 2017, **36**, 22.
33 Z. Skrott, M. Mistrik, K. K. Andersen, S. Friis, D. Majera, J. Gursky, T. Ozdian, J. Bartkova, Z. Turi, P. Moudry, M. Kraus, M. Michalova, J. Vaclavkova, P. Dzubak, I. Vrobel, P. Pouckova, J. Sedlacek, A. Miklovicova, A. Kutt, J. Li, J. Mattova, C. Driessen, Q. P. Dou, J. Olsen, M. Hajduch, B. Cvek, R. J. Deshaies and J. Bartek, *Nature*, 2017, **552**, 194–199.
34 W. Wu, L. Yu, Y. Pu, H. Yao, Y. Chen and J. Shi, *Adv. Mater.*, 2020, **32**, 2000542.
35 B. Cvek, *Drug Discovery Today*, 2012, **17**, 409–412.
36 Y. Ren, Y. Lin, J. Chen and Y. Jin, *Biol. Pharm. Bull.*, 2021, **44**, 1557–1564.
37 Z. Gao, Y. Li, Y. Zhang, P. An, F. Chen, J. Chen, C. You, Z. Wang and B. Sun, *Nanoscale*, 2020, **12**, 8139–8146.
38 Y. Chang, F. Wu, N. K. Pandey, L. Chudal, M. Xing, X. Zhang, L. Nguyen, X. Liu, J. P. Liu, W. Chen and Z. Pan, *ACS Appl. Bio Mater.*, 2020, **3**, 7147–7157.
39 P. E. Tawari, Z. Wang, M. Najlah, C. W. Tsang, V. Kannappan, P. Liu, C. McConville, B. He, A. L. Armesilla and W. Wang, *Toxicol. Res.*, 2015, **4**, 1439–1442.
40 W. Liu, H. Xiang, M. Tan, Q. Chen, Q. Jiang, L. Yang, Y. Cao, Z. Wang, H. Ran and Y. Chen, *ACS Nano*, 2021, **15**, 6457–6470.
41 D. J. Lewis, P. Deshmukh, A. A. Tedstone, F. Tuna and P. O'Brien, *Chem. Commun.*, 2014, **50**, 13334–13337.
42 S. Bakthavatsalam, M. L. Sleeper, A. Dharani, D. J. George, T. Zhang and K. J. Franz, *Angew. Chem., Int. Ed.*, 2018, **57**, 12780–12784.
43 Y. Sun, C. An, L. Wu, W. Zeng, J. Wang, Y. Wang, J. He, G. Gao and D. Ye, *ACS Nano*, 2021, **15**, 16298–16313.
44 A. Steinbrueck, A. C. Sedgwick, J. T. Brewster II, K.-C. Yan, Y. Shang, D. M. Knoll, G. I. Vargas-Zúñiga, X.-P. He, H. Tian and J. L. Sessler, *Chem. Soc. Rev.*, 2020, **49**, 3726–3747.
45 A. Mcmahon, W. Chen and F. Li, *J. Controlled Release*, 2020, **319**, 352–359.
46 Y. Jiang, H. Chen, T. Wang, F. Zhang, J. Shi, X. Kong and W. Chen, *ACS Appl. Nano Mater.*, 2022, **5**, 13069–13077.
47 L. Zhou, L. Yang, C. Yang, Y. Liu, Q. Chen, W. Pan, Q. Cai, L. Luo, L. Liu, S. Jiang, H. He, Y. Zhang, T. Yin and X. Tang, *Pharm. Res.*, 2018, **35**, 147.
48 Z. Skrott, D. Majera, J. Gursky, T. Buchtova, M. Hajduch, M. Mistrik and J. Bartek, *Oncogene*, 2019, **38**, 6711–6722.
49 Q.-H. Lan, C.-C. Du, R.-J. Yu, J. Zhai, Y. Shi, L. Kou, J. Xiao, C.-T. Lu, Y.-Z. Zhao and Q. Yao, *Int. J. Pharm.*, 2021, **607**, 120978.
50 M. Chang, M. Wang, M. Wang, M. Shu, B. Ding, C. Li, M. Pang, S. Cui, Z. Hou and J. Lin, *Adv. Mater.*, 2019, **31**, 1905271.
51 B. Ma, S. Wang, F. Liu, S. Zhang, J. Duan, Z. Li, Y. Kong, Y. Sang, H. Liu, W. Bu and L. Li, *J. Am. Chem. Soc.*, 2019, **141**, 849–857.
52 C. Wang, F. Cao, Y. Ruan, X. Jia, W. Zhen and X. Jiang, *Angew. Chem., Int. Ed.*, 2019, **58**, 9846–9850.
53 K. Lu, I. Psakhye and S. Jentsch, *Cell*, 2014, **158**, 549–563.
54 F. Tisato, C. Marzano, M. Porchia, M. Pellei and C. Santini, *Med. Res. Rev.*, 2010, **30**, 708–749.
55 Y. Zhang, G. Qi, X. Qu, B. Wang, K. Ma and Y. Jin, *Langmuir*, 2022, **38**, 584–592.
56 H.-X. Tang, C.-G. Liu, J.-T. Zhang, X. Zheng, D.-Y. Yang, R.-K. Kankala, S.-B. Wang and A.-Z. Chen, *ACS Appl. Mater. Interfaces*, 2020, **12**, 47289–47298.
57 H. Zhang, W. Tang, Q. Gong, X. Yang, Y. Sun, Z. Dai, Z. Hu and X. Zheng, *Nanoscale*, 2022, **14**, 13113–13122.
58 L. Hou, Y. Liu, W. Liu, M. Balash, H. Zhang, Y. Zhang, H. Zhang and Z. Zhang, *Acta Pharm. Sin. B*, 2021, **11**, 2016–2030.
59 Y. Li, W. Lu, Q. Huang, C. Li and W. Chen, *Nanomedicine*, 2010, **5**, 1161–1171.
60 L. Chudal, N. K. Pandey, J. Phan, O. Johnson, L. Lin, H. Yu, Y. Shu, Z. Huang, M. Xing, J. P. Liu, M.-L. Chen and W. Chen, *ACS Appl. Bio Mater.*, 2020, **3**, 1804–1814.
61 L. Chudal, N. K. Pandey, J. Phan, O. Johnson, X. Li and W. Chen, *Mater. Sci. Eng.*, 2019, **104**, 109979.
62 L. Li, L. H. Rashidi, M. Yao, L. Ma, L. Chen, J. Zhang, Y. Zhang and W. Chen, *Photodiagn. Photodyn. Ther.*, 2017, **19**, 5–14.